INTERNATIONAL JOURNAL FOR NUMERICAL METHODS IN FLUIDS
Int. J. Numer. Meth. Fluids 2001; **36**: 773–805 (DOI: 10.1002/fld.155)

Analysis of super compact finite difference method and application to simulation of vortex–shock interaction

Fu Dexun[a,]* and Ma Yanwen[b]

[a] *LNM, Institute of Mechanics, Chinese Academy of Sciences, Beijing, People's Republic of China*
[b] *LHD, Institute of Mechanics, Chinese Academy of Sciences, Beijing, People's Republic of China*

SUMMARY

Turbulence and aeroacoustic noise high-order accurate schemes are required, and preferred, for solving complex flow fields with multi-scale structures. In this paper a super compact finite difference method (SCFDM) is presented, the accuracy is analysed and the method is compared with a sixth-order traditional and compact finite difference approximation. The comparison shows that the sixth-order accurate super compact method has higher resolving efficiency. The sixth-order super compact method, with a three-stage Runge–Kutta method for approximation of the compressible Navier–Stokes equations, is used to solve the complex flow structures induced by vortex–shock interactions. The basic nature of the near-field sound generated by interaction is studied. Copyright © 2001 John Wiley & Sons, Ltd.

KEY WORDS: compressible Navier–Stokes equations; sound generation; super compact finite difference method; vortex–shock interaction

1. INTRODUCTION

For solving complex flow fields with multi-scale structures, attention must be paid to two important factors. One of them is to ensure that the effect of the physical diffusion must not be masked by numerical dissipations. This is especially important for directly simulating turbulent flows and aeroacoustic sound originating from disturbances of the pressure field with small amplitudes. Another important factor is to ensure that the phase speed of flow structures can be well approximated. For simulating the complex flow fields it is necessary that dispersion of physical acoustic waves can be approximated well in a wider range of wavenumbers. The commonly used second-order accurate schemes with limited number of grid points usually cannot give correct descriptions of both the amplitude and phase speed for the small-scale flow field structures. From linear analysis and numerical experiments it can be seen that the higher-order accurate method can give better resolution of the complex flow fields with multi-scale structures.

---

* Correspondence to: LNM, Institute of Mechanics, Chinese Academy of Sciences, Beijing 100080, People's Republic of China.

Received January 2000
Revised June 2000

There are three kinds of finite difference methods with high-order accuracy. They are the traditional finite difference schemes [1], symmetrical and upwind compact schemes [2–4] and super compact difference schemes [5,6]. For the traditional difference schemes it is difficult to increase the order of accuracy of approximation. When higher-order accurate schemes are needed one has to enlarge the stencil of grid points. This leads to a difficult treatment of the boundary conditions and difference approximations at the points next to the boundaries. The situation is better for the compact schemes; the stencil is smaller than that of the traditional difference schemes. However, for higher-order compact difference schemes the stencil still has to be enlarged and it is difficult to get closed formulae for arbitrarily high accurate schemes. In References [5,6], the so-called super compact finite difference method (SCFDM) is developed. With the SCFDM, arbitrarily high accuracy can be obtained only with two or three grid points.

In the present paper, the SCFDM is presented, the behaviour of the numerical solution with the SCFDM is analysed and then the method is used to simulate vortex–shock interactions. Recently, researchers have paid more attention to problems of vortex–shock interactions. It is known that shock can change the coherent structures that play important roles in mixing for supersonic combustion problems. The vortex–shock interaction is also a good model for understanding sound generation. In Reference [7] a two-dimensional weak vortex–shock interaction is studied numerically, with the sixth-order accurate Padé spatial discretization. The same problem is solved with the same scheme as in Reference [8], but the emphasis is on the sound field generated by vortex–shock interactions. To obtain better resolution of the shock, 1044 (x-direction) $\times$ 1170 (y-direction) mesh grid points are used [8]. The vortex–shock interaction problem is also studied numerically in References [9–12], and basic shock structures in vortex–shock interaction are discussed. In present paper an accuracy analysis of the SCFDM is given and the method is applied to simulate the same problem. Further details are given.

The method of discretization is given in Section 2, the mesh grid and the boundary and initial conditions are given in Section 3 and the computed results are presented in Sections 4 and 5.

2. SUPER COMPACT FINITE DIFFERENCE METHOD (SCFDM)

The difficulties in correctly simulating aeroacoustic field include a large disparity between the energy levels of the unsteady flow fluctuations and the sound, and an even larger disparity in length scales. Also, the characteristic flow speed is small compared with the speed of sound propagation in the medium. In order to correctly simulate this kind of flow structure, it is necessary that the numerical method has small dispersion and dissipation errors, and can capture the multi-scale structures. With the limitation of computer resources, high-order accurate methods are preferred. With the same number of the mesh grid points, the high-order schemes have a wider range of wavenumbers for correct simulation. In high-order schemes with the same order of accuracy, the SCFDM developed by the authors in References [5,6] has higher resolving efficiency. In this section we will present the SCFDM and analyse the accuracy of numerical solutions.

2.1. Method

Define n-dimensional vectors

$$F=[f^{\langle 1\rangle},f^{\langle 3\rangle},\ldots,f^{\langle 2N-1\rangle}]^T$$

$$e_1=[1,0,\ldots,0]^T$$

and $N\times N$ matrices

$$A=\begin{bmatrix} \frac{1}{1!} & \frac{1}{3!} & \frac{1}{5!} & \cdots & \frac{1}{[2N-1]!} \\ 0 & \frac{1}{2!} & \frac{1}{4!} & \cdots & \frac{1}{[2(N-1)]!} \\ 0 & 0 & \frac{1}{2!} & \cdots & \frac{1}{[2(N-2)]!} \\ \vdots & \vdots & \vdots & \vdots & \vdots \\ 0 & 0 & 0 & \cdots & \frac{1}{4!} \\ 0 & 0 & 0 & \cdots & \frac{1}{2!} \end{bmatrix}, \qquad L=\begin{bmatrix} 0 & 0 & 0 & \cdots & 0 & 0 \\ 1 & 0 & 0 & \cdots & 0 & 0 \\ 0 & 1 & 0 & \cdots & 0 & 0 \\ \vdots & \vdots & \vdots & \cdots & \vdots & \vdots \\ 0 & 0 & 0 & \cdots & 0 & 0 \\ 0 & 0 & 0 & \cdots & 1 & 0 \end{bmatrix}$$

where

$$f^{\langle l\rangle}=\Delta x^l\frac{\partial^l f}{\partial x^l} \tag{2.1}$$

The simpler three-point SCFDM for approximation of the odd derivatives is expressed as follows:

$$-\frac{1}{2}LF_{j-1}+(L+A)F_j-\frac{1}{2}LF_{j+1}=\delta_x^0 f_j e_1 \tag{2.2}$$

where

$$\delta_x^0=\frac{\delta_x^+ + \delta_x^-}{2}, \qquad \delta_x^\pm f_j=\mp(f_j-f_{j\pm 1}) \tag{2.3}$$

If the point function f_i is given we can get all $f_j^{\langle 2l-1\rangle}$, where $l=1,2,\ldots,N$. The relation $f^{\langle 2l-1\rangle}/\Delta x^{2l-1}$ approximates the derivative $\partial^{2l-1}f/\partial x^{2l-1}$, with accuracy of order $2(N-l+1)$. In the present computation $N=3$ is used to compute $f^{\langle 1\rangle}/\Delta x$, which approximates $\partial f/\partial x$ with sixth-order accuracy.

For computing the discrete approximation of the second derivative $\partial^2 f/\partial x^2$ we define

$$S=[f^{\langle 2\rangle},f^{\langle 4\rangle},\ldots,f^{\langle 2N\rangle}]^T$$

$$B=\begin{bmatrix} \frac{1}{2!} & \frac{1}{4!} & \frac{1}{6!} & \cdots & \frac{1}{[2N]!} \\ 0 & \frac{1}{2!} & \frac{1}{4!} & \cdots & \frac{1}{[2(N-1)]!} \\ 0 & 0 & \frac{1}{2!} & \cdots & \frac{1}{[2(N-2)]!} \\ \vdots & \vdots & \vdots & \cdots & \vdots \\ 0 & 0 & 0 & \cdots & \frac{1}{4!} \\ 0 & 0 & 0 & \cdots & \frac{1}{2!} \end{bmatrix}$$

The difference equations with the SCFDM for obtaining the difference approximation for the even derivatives in the vector form are expressed as

$$-\frac{1}{2}LS_{j-1}+(L+B)S_j-\frac{1}{2}LS_{j+1}=\frac{1}{2}\delta_x^2 f_j e_1 \tag{2.4}$$

where

$$\delta_x^2=\delta_x^+\delta_x^- \tag{2.5}$$

The matrix L and the vector e_1 are defined as before. The relation $f^{\langle 2l\rangle}/\Delta x^{2l}$ approximates the derivatives $\partial^{2l}f/\partial x^{2l}$ with accuracy of order $2(N-l+1)$.

2.2. Accuracy analysis

In References [5,6] the accuracy of the SCFDM is not compared with other schemes. In this section, the accuracy of the sixth-order accurate SCFDM for the first derivative is analysed and compared with the sixth-order accurate traditional and the symmetrical compact difference approximation developed in References [1,2].

The sixth-order accurate traditional difference approximation is expressed as

$$F_j = \frac{1}{60}[45(f_{j+1} - f_{j-1}) - 9(f_{j+2} - f_{j-2}) + f_{j+3} - f_{j-3}] \tag{2.6}$$

where $F_j/\Delta x$ is an approximation of $(\partial f/\partial x)_j$.

The sixth-order compact difference approximation is

$$\frac{1}{5}F_{j+1} + \frac{3}{5}F_j + \frac{1}{5}F_{j-1} = \frac{14}{15}\delta_x^0 f_j + \frac{1}{30}\delta_x^0(f_{j+1} - f_{j-1}) \tag{2.7}$$

There are two ways to estimate the formal accuracy of schemes. One of them is to consider the truncation errors (T.E.). The truncation errors for the traditional, compact and super compact difference approximations with sixth-order accuracy are as follows:

traditional difference approximation

$$\text{T.E.} = 2160\frac{\Delta x^6}{7!}\frac{\partial^7 f}{\partial x^7} \tag{2.8}$$

compact difference approximation

$$\text{T.E.} = \frac{12}{5}\frac{\Delta x^6}{7!}\frac{\partial^7 f}{\partial x^7} \tag{2.9}$$

super compact difference approximation

$$\text{T.E.} = \frac{\Delta x^6}{7!}\frac{\partial^7 f}{\partial x^7} \tag{2.10}$$

From the above-listed truncation errors it can be seen that the compact difference approximation is better than the traditional approximation, and the super compact difference approximation is better than the compact difference approximation.

Another way for estimation of the resolving efficiency is by using Fourier analysis [2]. The modified wavenumbers for the sixth-order accurate traditional, compact and super compact difference approximation are [2,4,6]

traditional difference approximation

$$K_i(\alpha) = \frac{3}{2}\sin(\alpha) - 0.3\sin(2\alpha) + \frac{1}{30}\sin(3\alpha) \tag{2.11}$$

compact difference approximation

$$K_i(\alpha) = \frac{28\sin(\alpha) + \sin(2\alpha)}{6[3 + 2\cos(\alpha)]} \tag{2.12}$$

super compact difference approximation

$$K_i(\alpha) = \frac{5\sin(\alpha)\,[5 + \cos(\alpha)]}{16 + \cos(\alpha)[13 + \cos(\alpha)]} \tag{2.13}$$

where $\alpha = K\Delta x$. Variations of the modified wavenumbers $K_i(\alpha)$ versus α are given in Figure 1(a). Figure 1(b) gives the variations of group velocity of wave packets defined by $D(\alpha) = \mathrm{d}K_i(\alpha)/\mathrm{d}\alpha$ for the difference approximation [4]. The group velocity defines the speed and the

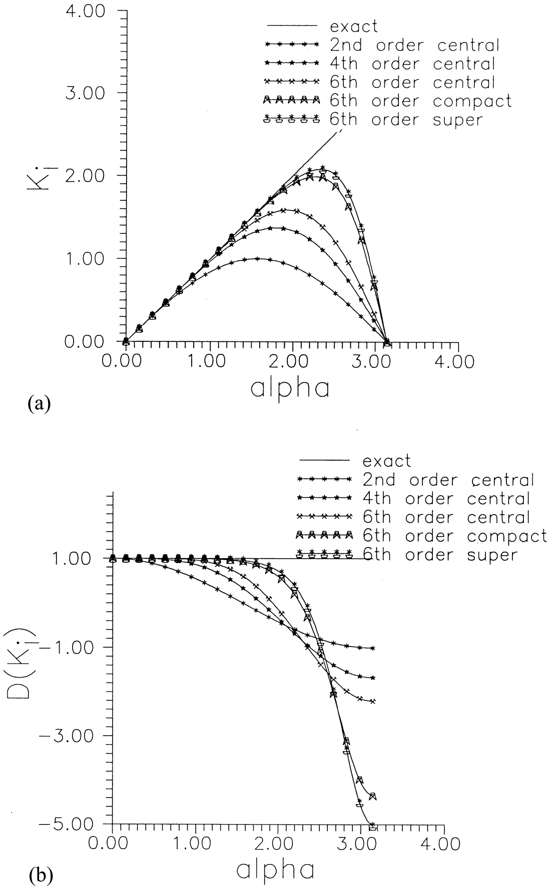

Figure 1. (a) Variation of modified wavenumbers versus $\alpha = k\Delta x$. (b) Variation of group velocity of wave packets versus $\alpha = k\Delta x$.

direction of propagation of wave packets in numerical solutions. For the exact solution, $K_i(\alpha) = \alpha$, $D(\alpha) = 1.0$. From Figure 1 it can be seen that the super compact difference approximation has better resolving efficiency.

In multi-dimensional problems, the dispersion effect appears in the form of anisotropy. In order to analyse the anisotropic effect, we consider the following model equation:

$$\frac{\partial u}{\partial t} + a\frac{\partial u}{\partial x} + b\frac{\partial u}{\partial y} = 0, \quad a,\ b = \text{constant} \tag{2.14}$$

with the initial condition

$$u(x, 0) = \exp\{\mathrm{i}[\mathbf{K}\cdot\mathbf{X}]\} \tag{2.15}$$

where $\mathbf{K} = [k_1, k_2]$, $\mathbf{X} = [x, y]^T$ and k_1, k_2 are wavenumbers in the x- and y-directions respectively. Define

$$\mathbf{I} = \left[\frac{a}{(a^2 + b^2)^{1/2}}, \frac{b}{(a^2 + b^2)^{1/2}}\right]^T$$

or

$$\mathbf{I} = [\cos\theta,\ \sin\theta]^T$$

where θ is the azimuthal angle.

The exact solution for Equation (2.14) with initial condition (2.15) can be expressed as

$$u(\mathbf{X}, t) = \exp\{\mathrm{i}[\mathbf{K}\cdot\mathbf{X} - (a^2 + b^2)^{1/2}\mathbf{K}\cdot\mathbf{I}t]\}. \tag{2.16}$$

The semi-discrete approximation for Equation (2.14)

$$\frac{\partial u}{\partial t} + a\frac{F_i}{\Delta x} + b\frac{F_j}{\Delta y} = 0 \tag{2.17}$$

with initial condition (2.15) has the exact solution as follows:

$$u(\mathbf{X}, t) = \exp\{-(a^2 + b^2)^{1/2}\mathbf{K}\cdot\mathbf{I}'_r t\}\cdot\exp\{\mathrm{i}\mathbf{K}\cdot[\mathbf{X} - (a^2 + b^2)^{1/2}\mathbf{I}'_i t]\}$$

$$\mathbf{I}'_r = \left[\cos\theta\frac{K_r^{(1)}}{\alpha}, \sin\theta\frac{K_r^{(2)}}{\beta}\right]^T, \quad \alpha = k_1\Delta x$$

$$\mathbf{I}'_i = \left[\cos\theta\frac{K_i^{(1)}}{\alpha}, \sin\theta\frac{K_i^{(2)}}{\beta}\right]^T, \quad \beta = k_2\Delta y \tag{2.18}$$

where $K_r^{(1)}$, $K_i^{(1)}$, vectors $\mathbf{I}_i'$ and $\mathbf{I}_r'$ are functions of α and β. $\mathbf{I}_i'$ is related to numerical dispersions and $\mathbf{I}_r'$ is related to numerical dissipations. For different schemes $\mathbf{I}_r'$ and $\mathbf{I}_i'$ are different. Suppose the scheme is non-dissipative, $\mathbf{I}_r'=0$, $a=b=1$ and $\Delta x=\Delta y=h$. The dispersion relation for the exact solution can be obtained from Equation (2.16)

$$\omega_e=(a^2+b^2)^{1/2}\mathbf{K}\cdot\mathbf{I}h=\alpha+\beta \tag{2.19}$$

The dispersion relation for Equation (2.18) is

$$\omega_h=(a^2+b^2)^{1/2}\mathbf{K}\cdot\mathbf{I}_i'h=K_i(\alpha)+K_i(\beta) \tag{2.20}$$

The contours $\omega_e=$constant for an exact solution is given in Figure 2(a) and contours $\omega_h=$constant for the above-listed sixth-order accurate schemes are given in Figure 2(b)–(d).

From Figure 2 we see that there are serious anisotropic effect for high wavenumbers. The direction normal to the lines of $\omega=$constant shows the propagation direction of wave packets. In the numerical solution we have wrong propagation speeds for very high wavenumbers. Comparing Figure 2(b)–(d) with Figure 2(a), we see that within the sixth-order accurate schemes the SCFDM has better resolving efficiency.

From Equations (2.2), (2.6) and (2.7) we see that the traditional difference approximation has the largest stencil of mesh grid points and the SCFDM has the smallest. With the SCFDM, the same difference relations can be used for all the interior points and the difference approximations do not need to be treated specially at the near-boundary points.

2.3. Time integration

The above sixth-order accurate SCFDM with three-stage Runge–Kutta method is used to solve the two-dimensional compressible Navier–Stokes equations for the simulation of vortex–shock interactions. After spatial discretization we obtain the difference equation

$$\frac{\mathrm{d}U}{\mathrm{d}t}=L_h(U) \tag{2.21}$$

The three-stage Runge–Kutta method in time integration is as follows:

$$U^{(1)}=U^n+\Delta tL_h(U^n) \tag{2.22a}$$

$$U^{(2)}=\frac{3}{4}U^n+\frac{1}{4}[U^{(1)}+\Delta tL_h(U^{(1)})] \tag{2.22b}$$

$$U^{n+1}=\frac{1}{3}U^n+\frac{2}{3}[U_j^{(2)}+\Delta tL_h(U^{(2)})] \tag{2.22c}$$

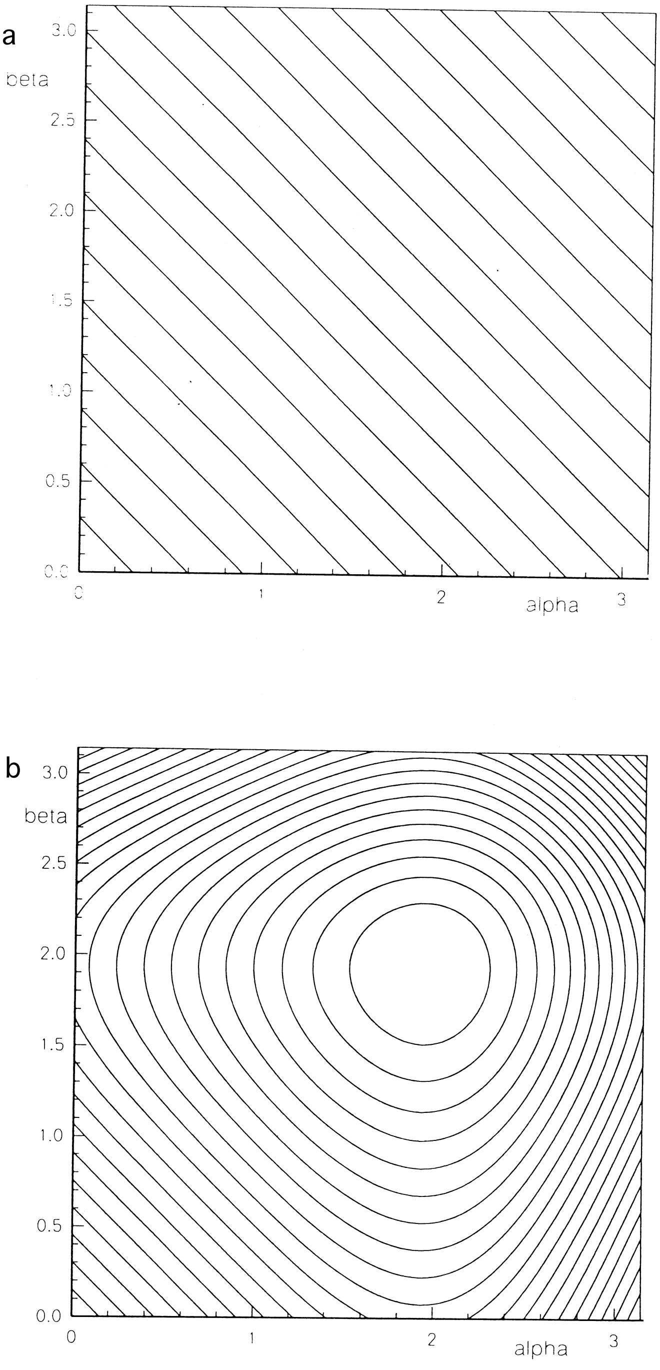

Figure 2. Anisotropic effect coutours of dispersion relations: (a) exact solution; (b) sixth-order traditional scheme; (c) sixth-order compact scheme; (d) sixth-order SCFDM.

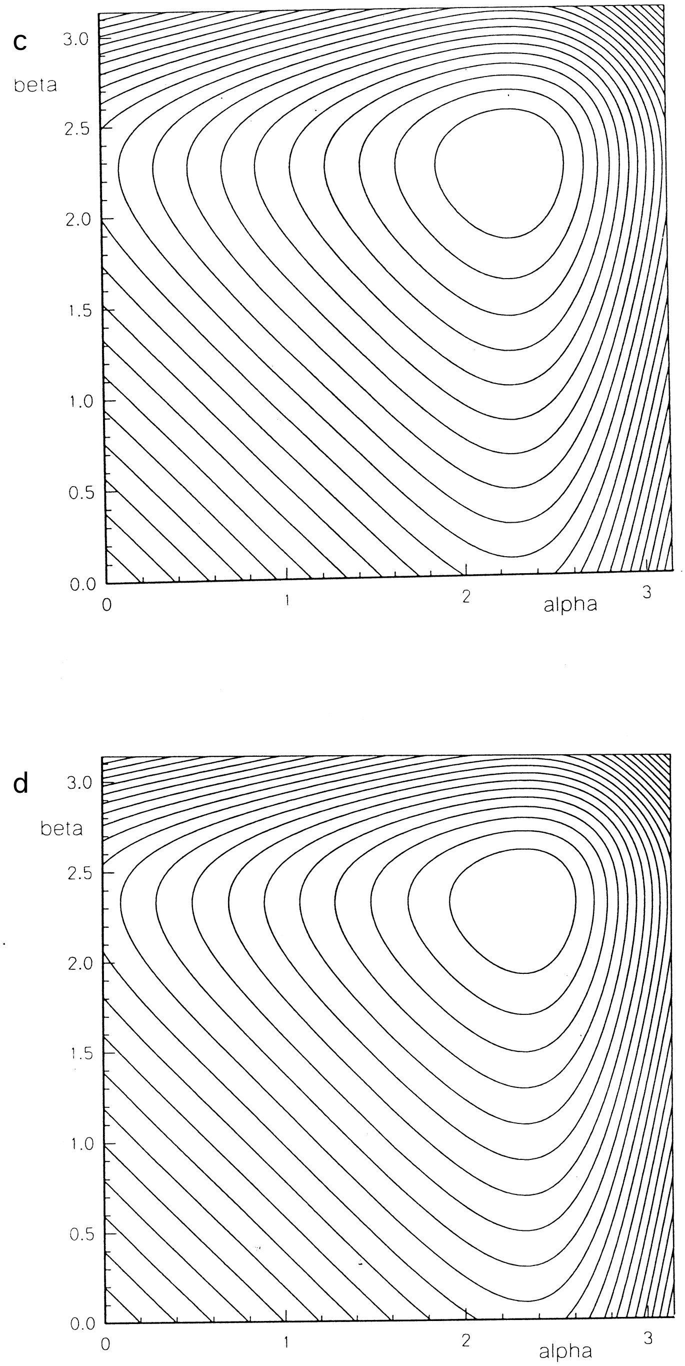

Figure 2 (*Continued*)

3. MESH GRID SYSTEM, BOUNDARY AND INITIAL CONDITIONS

A standing shock is initially located at $x = -0.1$. A vortex or a pair of vortices is initially located upstream and is going through the shock. The computational domain is a rectangular $-6.0 \leq x \leq 20.8$, $-12 \leq y \leq 12$. Near the origin of co-ordinates $(0, 0)$ uniform fine mesh is used in both the x- and y-directions. In the far field from the origin, a uniform coarse mesh is used, and between the fine and the coarse mesh grid, the spatial increment is variable. The co-ordinate transformation is continuous, and has continuous derivatives. In all computations $\Delta x_{\min} = 0.24^{-2}$, $\Delta x_{\max} = 0.1$, $\Delta y_{\min} = 0.23^{-2}$ and $\Delta y_{\max} = 0.12$. The number of grid points is 601×601.

In the computation periodic boundary conditions are used at upper and lower boundaries, and non-reflecting conditions are imposed at the downstream boundary.

Initial data consist of a streamwise supersonic flow with a vertical shock and a vortex located upstream from the discontinuity. The uniform incoming flow has Mach number M_∞. The vortex is assumed to have velocity distributions [8] as follows:

$$u_\theta(r) = M_v r \exp[(1 - r^2)/2] \tag{3.1a}$$

$$u_r = 0 \tag{3.1b}$$

where r is the distance normalized by the radius of the vortex from the considered point to the centre of vortex. The tangential velocity component $u_\theta(r)$ and the radial velocity component u_r are normalized by the upstream sound velocity a_∞. The Mach number M_v of the vortex is defined by $M_v = u_{\theta\max}/a_\infty$, where $u_{\theta\max}$ is the maximum tangential velocity at $r = 1$. The initial pressure and the density distributions are expressed by [8]

$$P(r) = \frac{1}{\gamma}\left[1 - \frac{\gamma - 1}{2} M_v^2 \exp(1 - r^2)\right]^{\gamma/(\gamma - 1)} \tag{3.2a}$$

$$\rho(r) = \left[1 - \frac{\gamma - 1}{2} M_v^2 \exp(1 - r^2))\right]^{\gamma/(\gamma - 1)} \tag{3.2b}$$

where γ denotes the ratio of specific heats, $\gamma = 1.4$. The density ρ and the pressure P are normalized by ρ_∞ and the sound velocity a_∞, where the subscript ∞ denotes the quantity upstream of the shock.

4. SINGLE VORTEX–SHOCK INTERACTION

4.1. Computed results

Two cases are computed for a single vortex–shock interaction. The flow parameters for the first case (case A) are $M_\infty = 1.2$, $M_v = 0.25$, $Re = 800$, and for the second case (case B) are $M_\infty = 1.29$, $M_v = 0.39$, $Re = 800$. For both cases the initial shock is located at $x = -0.1$, and the centre of the vortex is initially located at the point $(-3, 0)$. The vortex rotates in a clockwise direction.

The sound field is defined by the pressure difference $\Delta P = (P - P_s)/P_\infty$, where P_s is the undisturbed pressure behind the shock. The computed sound fields (contours of ΔP) for case A are given in Figure 3(a)–(c) at $t = 2.0$, 5.0 and 7.0. Figure 3(d) gives the density field at $t = 7.0$. The solid lines for the pressure difference means $\Delta P > 0$, and it is denoted by the symbol '$+$' in the figures. The dash lines means $\Delta P < 0$, and it is denoted by symbol '$-$'. The computed sound fields for case B are given in Figure 4 and the density and Mach number contours are given in Figure 5.

Initially from the sound field we can see the outer precursor quadrupolar nature of the sound and the second sound following the precursor. Also, we can see that the sound consists of two parts. The first part mainly concentrates near the vortex and moves together with the vortex. It only has transportation characteristics and does not propagate away from the vortex (Figures 3 and 4). It is called pseudo-sound. The second part propagates away from the vortex with sound speed. That is the source of noises.

4.2. Analysis of sound generation

A schematic diagram of the flow field structures behind the shock during the time of vortex–shock interaction is given in Figure 6. When the vortex starts to interact with the shock, the velocity field of the vortex is added and the shock is convected toward the downstream by a higher streamwise velocity, $u_\infty + u_\theta$, in the upper part of the plane, and toward upstream by a lower streamwise velocity, $u_\infty - u_\theta$, in the lower part of the flow field. Therefore, the shock shape is deformed as shown in Figure 6. The deformation process can be seen clearly in Figures 3 and 4. At the early stage of interaction, the shock is stretched symmetrically according to $y = 0$.

Consider the flow structure in the upper plane behind the shock. It is obvious that $\Delta P > 0$ behind the shock in the zone near the point B (Figure 6) because of a higher upstream incoming Mach number $M_\infty + M_v$. Moreover, by oblique shock theory, from the shock shape it can be seen that in zones $\overline{bcd}$ and $\overline{defgh}$ behind the shock, the flow is going towards the zone near point B. This means that the flow is compressed in the vicinity of point B. This compression phenomenon can be observed in Figures 3(a) and 4(a). At the same time we have rarefaction in the area near point C because of the lower velocity upstream of the shock and the flow direction near zones $\overline{efg}$ and $\overline{ijk}$ behind the shock. That is, the flow is going towards the upper-right behind $\overline{efg}$ and towards the lower-right behind $\overline{ijk}$. With similar analysis we know that the rarefaction is near zone A and the compression is near zone D behind the shock. These rarefaction and compression are much weaker compared with those in zones C and B behind the shock. The reason is weaker interaction of the outer part of the vortex with the shock and the one-side effect of compression in zone D and rarefaction in zone A. At this moment, due to deformation of the shock, the precursor quadrupolar nature of the sound is formed initially. It can be seen in Figures 3(a) and 4(a).

When the centre of the vortex just goes through the shock by using the normal shock relations we can get the pressure P_d at point d and P_h at point h behind the shock (Figure 6). The pressure difference between points d and h is

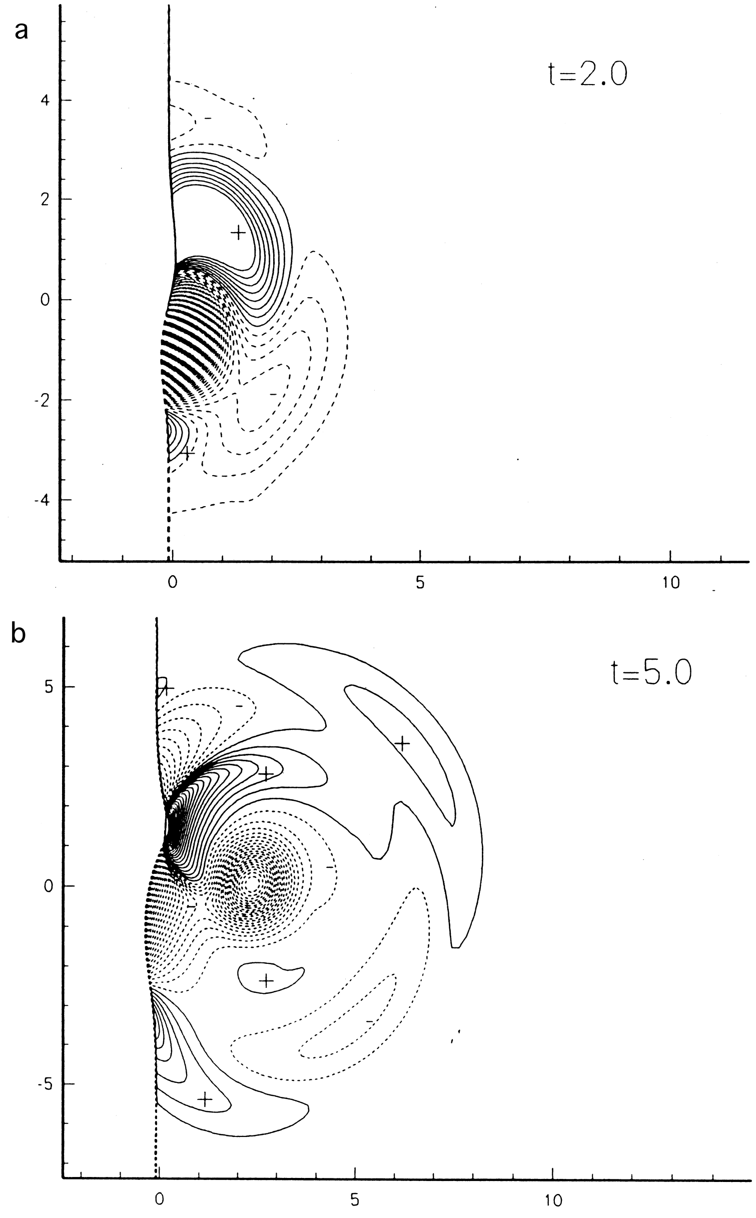

Figure 3. Time development of flow field for case A: (a) pressure field, $-0.5 \leq \Delta P \leq 0.15$, 80 levels; (b) pressure field, $-0.45 \leq \Delta P \leq 0.25$, 80 levels; (c) pressure field, $-0.5 \leq \Delta P \leq 0.125$, 80 levels; (d) density contours, $1.001 \leq \rho \leq 1.42$, 80 levels.

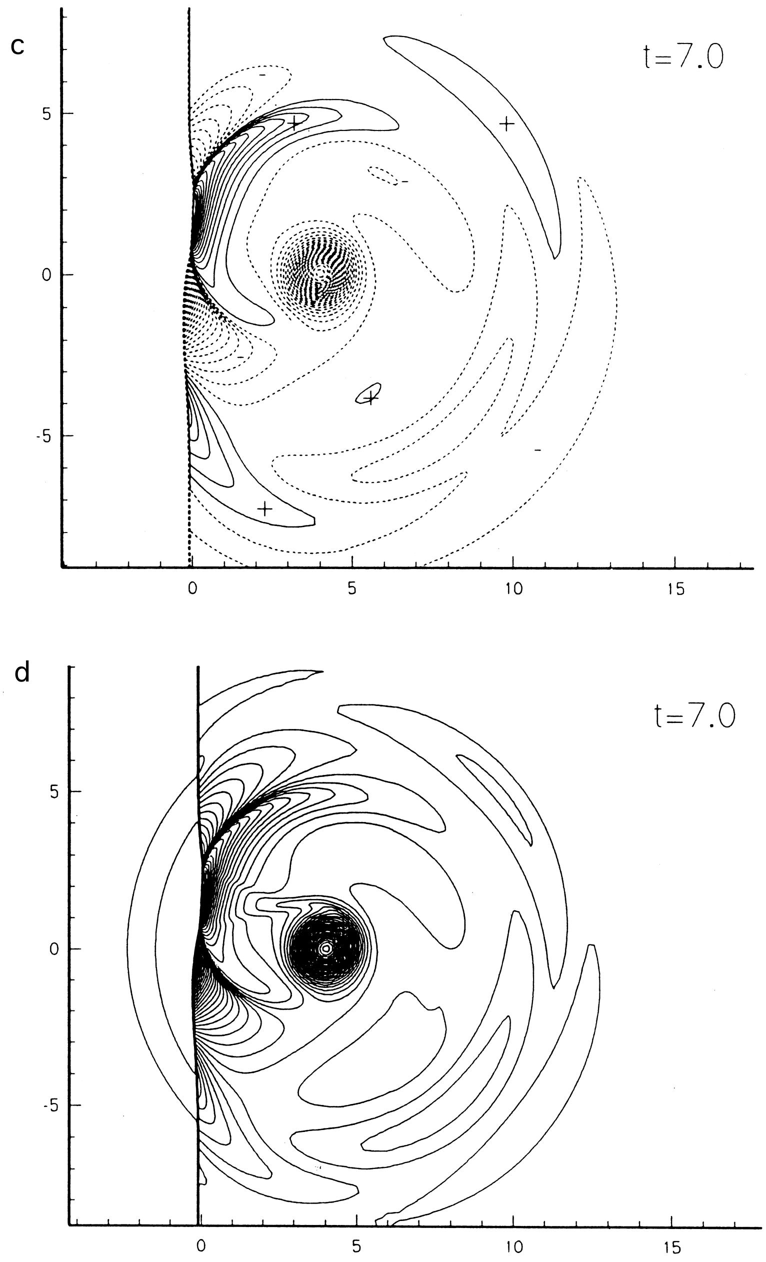

Figure 3 (*Continued*)

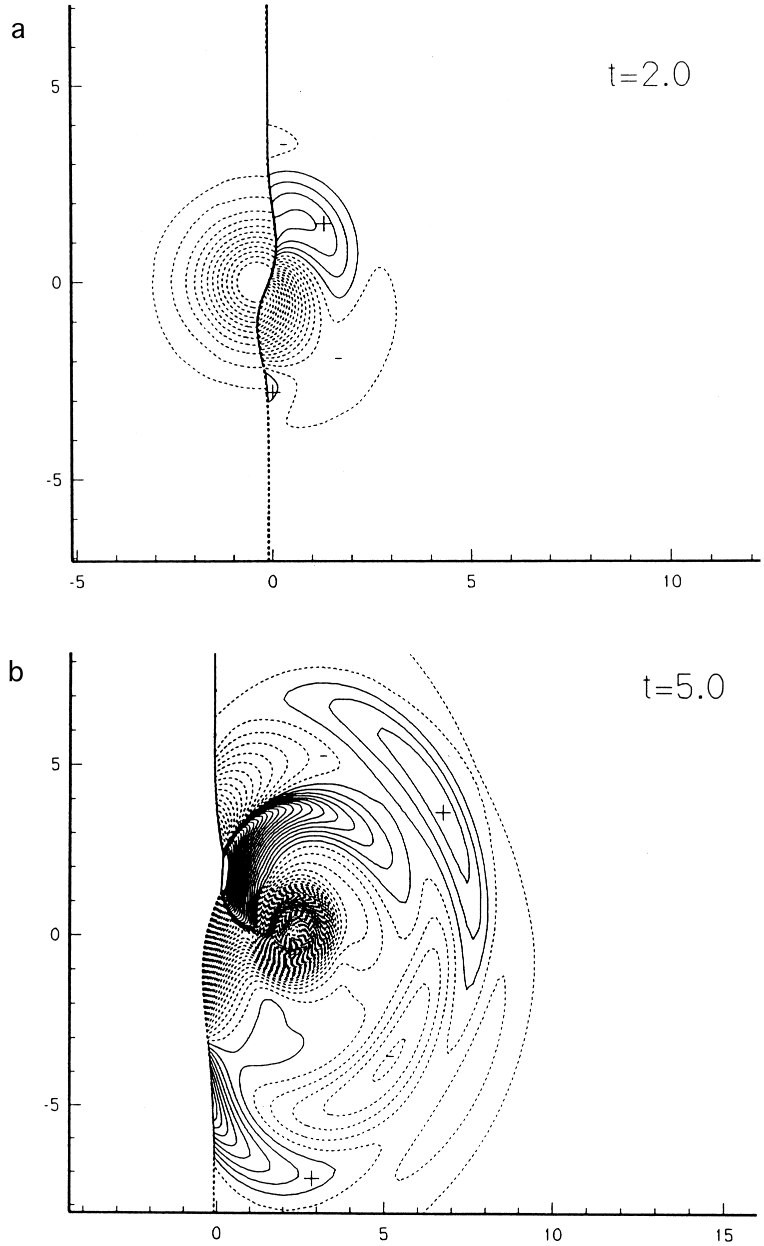

Figure 4. Time development of pressure field for case B: (a) $-0.5 \le \Delta P \le 0.5$, 80 levels; (b) $-0.5 \le \Delta P \le 0.3$, 80 levels; (c) $-0.6 \le \Delta P \le 0.2$, 80 levels; (d) $-0.3 \le \Delta P \le 0.12$, 60 levels.

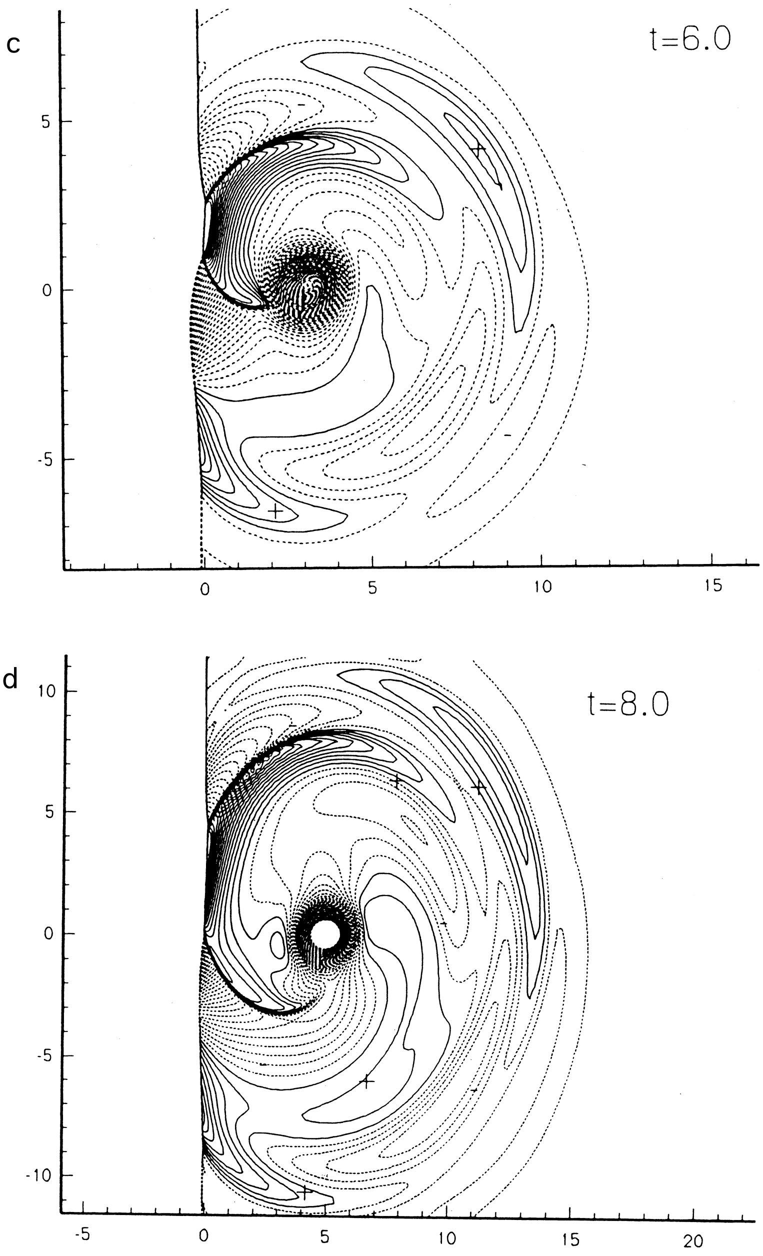

Figure 4 (*Continued*)

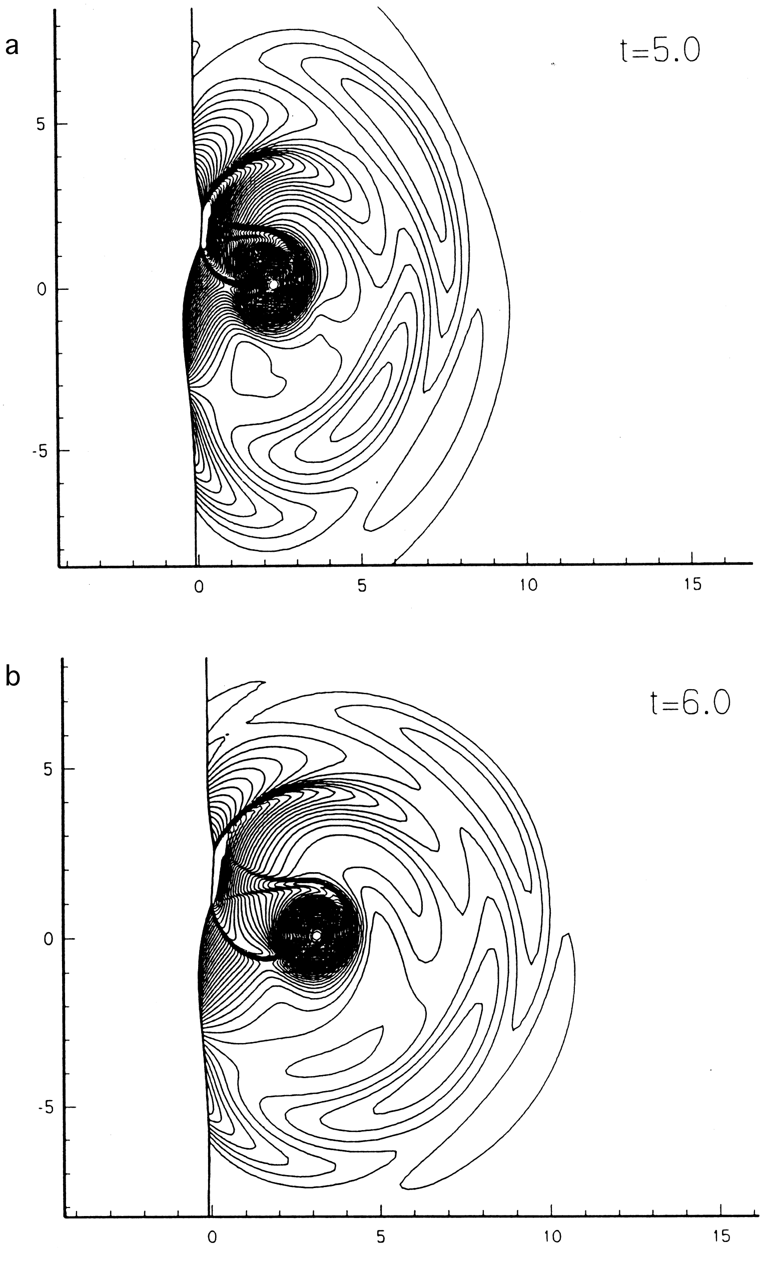

Figure 5. Time development of flow field for case B: (a) density contours, $1.2 \leq \rho \leq 1.65$, 80 levels; (b) density contours, $1.1 \leq \rho \leq 1.6$, 80 levels; (c) Mach number contours, $-0.5 \leq M_a - 1.0 \leq 0.5$, 80 levels; (d) Mach number contours, $-0.6 \leq M_a - 1.0 \leq 0.28$, 80 levels.

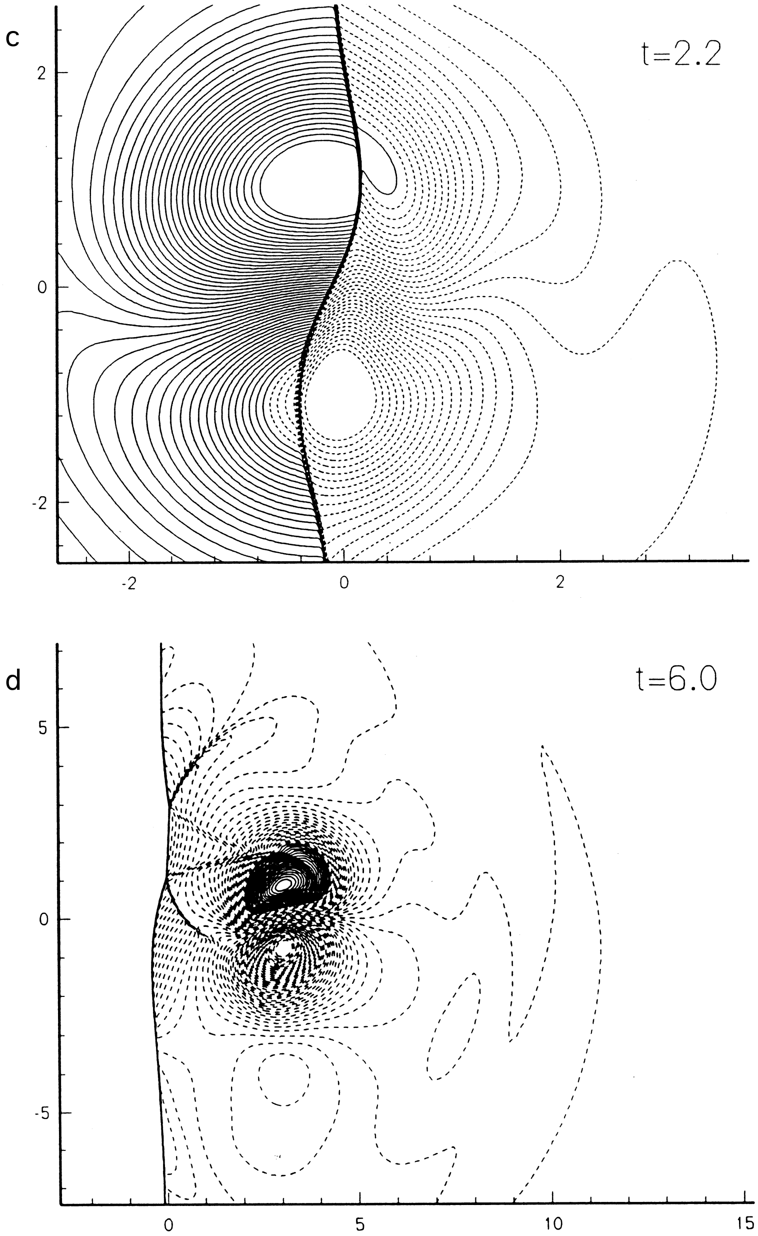

Figure 5 (*Continued*)

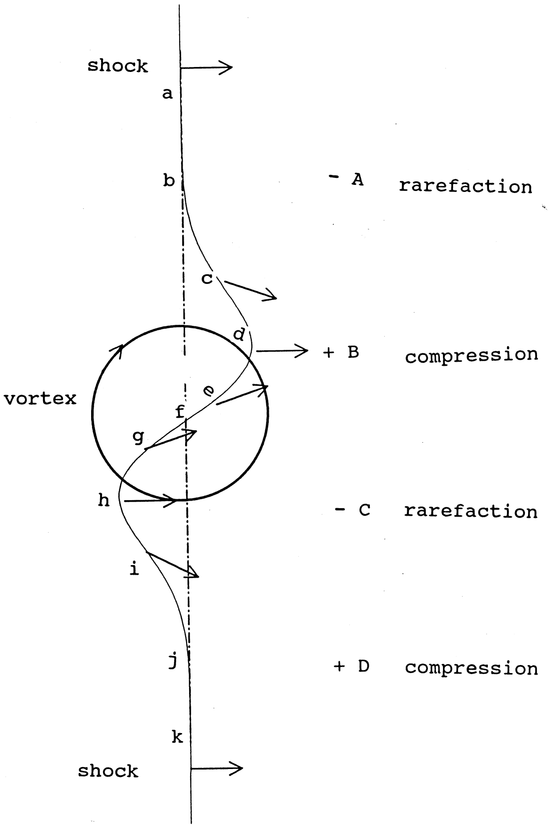

Figure 6. Schematic diagram of single vortex–shock interaction.

$$\Delta P_{dh}/P_{\infty} = \frac{8\gamma}{\gamma - 1} u_{\infty} u_{v} \tag{4.1}$$

From Equation (4.1) it can be seen that the variation in the y-direction behind the shock depends on the incoming velocity and the rotating velocity of the vortex. Because of different strengths of the shock in the y-direction due to different incoming Mach numbers with time integration, at the later time of interaction the deformation of the shock becomes unsymmetrical (see Figures 3 and 4). During the time of unsymmetrical deformation of the shock, the second quadrupolar nature of the sound, which follows the first one, is formed (Figures 3(b) and 4(b)). Also we can see non-uniform propagation characteristics of the sound field due to pressure gradient in the y-direction.

4.3. Structures of discontinuities

In cases A and B in the lower plane upstream of the shock we have incoming velocity $u_\infty - u_v$. In the flow field there is a sub-domain in which the incoming Mach number $M_\infty - M_v$ is less than 1. That is, the incoming flow is subsonic. In this case, the lower part of the shock is broken when the centre of the vortex goes across the shock. It is the residue of what was a shock wave. This can be seen in Figure 5(c) clearly. In the figure the dash lines show the region of subsonic flow, and the solid lines show the region of supersonic flow.

When the centre of the vortex goes through the shock, the deformed shock starts to restore and the broken shock is soon recovered. After that the secondary discontinuities with a cusp between the compression zone and the rarefaction zone near point B (Figure 6) is formed due to pressure gradients in the y-direction and vortex rotation. These discontinuities are called secondary shocks, as in References [7–10]. Both secondary discontinuities attach to the main shock near point B. One of the secondary discontinuities touches the vortex and is sustained by vortex rotation after vortex away from the shock, and another one will decay with increase of moving distance of the shock. These secondary discontinuities can be seen clearly in Figures 3(c) and 4(b). In both sides of these discontinuities the flows are subsonic (Figure 5). The strength of the secondary discontinuities depends on pressure difference ΔP_{dh} in Equation (4.1). For $M_1 > 1$ when ΔP_{dh} is large enough, the secondary discontinuities will be shock. This can be seen clearly in the case of a pair of vortices–shock interaction in the next section (see Figures 7(b) and 8(a)). From Figure 4(b) and (c) we see that the upper branch follows the circulation of the vortex and decays as the structure moves away from the shock. The lower branch is stronger and embedded in the rotating vortex. From Figure 4(b) and (c) it can also be seen that the vortex rotates across the lower branch of the secondary discontinuities.

During the time of formation of the secondary discontinuities from density contours (case B, Figure 5(a) and (b)), we can see two slip lines emerging from the vortex and attaching to the main shock. This kind of discontinuity cannot be seen in the corresponding pressure difference contours in Figure 4(b) and (c). Formation of the slip lines is due to interaction between the secondary discontinuities and the main shock.

5. A PAIR OF VORTICES-SHOCK INTERACTION

The flow parameters in computation for the case of a pair of vortice–shock interaction are $Re = 400$, $M_\infty = 1.2$ and $M_v = 0.5$. The shock initially is located at $x = -0.1$ as for the case of a single vortex–shock interaction. From Equation (4.1) it can be seen that in this case the flow disturbance behind the shock is stronger when comparing with cases A and B. The centre of the upper vortex initially is located at the point $(-3, 2)$, and the centre of the lower vortex is at the point $(-3, -2)$. For the first case (case C), near the central line $y = 0$, the flows of both upper and lower vortices are rotating positive towards the x-direction. For the second case (case D), near $y = 0$, the flows are rotating negative towards the x-direction. In these computations there are vortices–shock and vortex–vortex interactions.

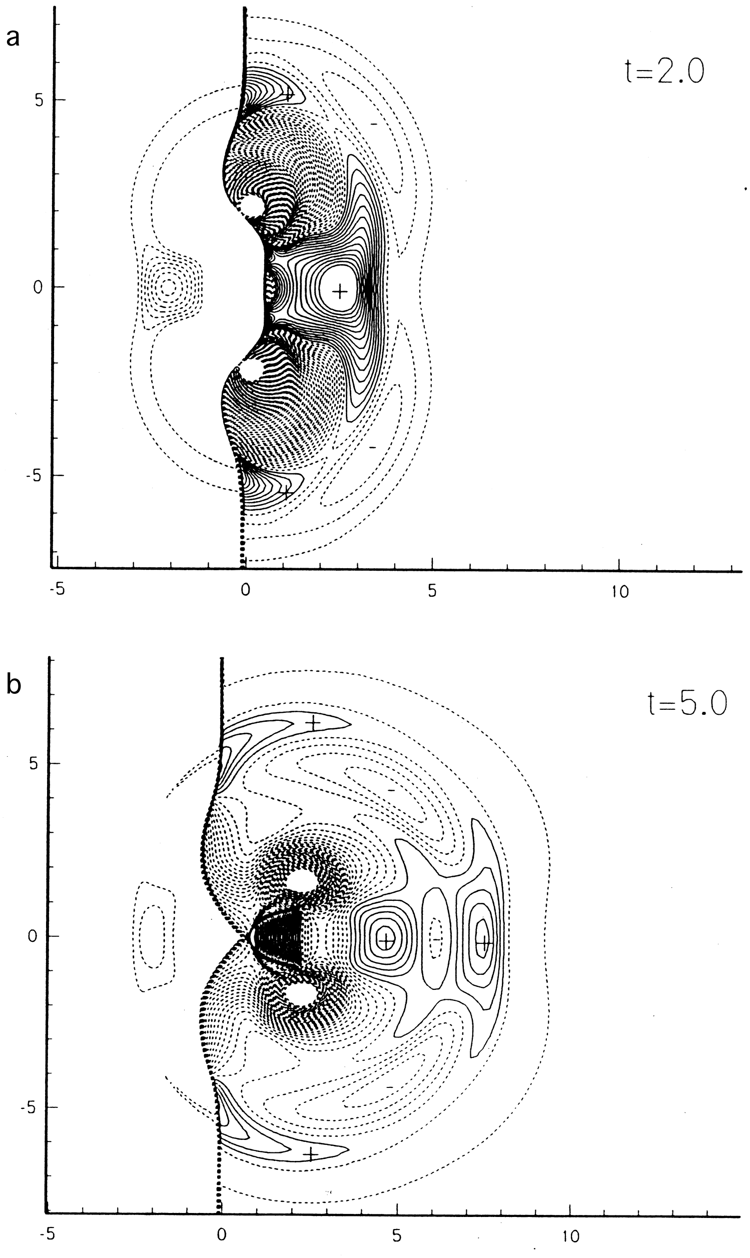

Figure 7. Time development of pressure field for case C: (a) $-0.5 \leq \Delta P \leq 0.1$, 80 levels; (b) $-0.5 \leq \Delta P \leq 0.6$, 70 levels; (c) $-0.5 \leq \Delta P \leq 0.25$, 50 levels; (d) $-0.5 \leq \Delta P \leq 0.12$, 50 levels.

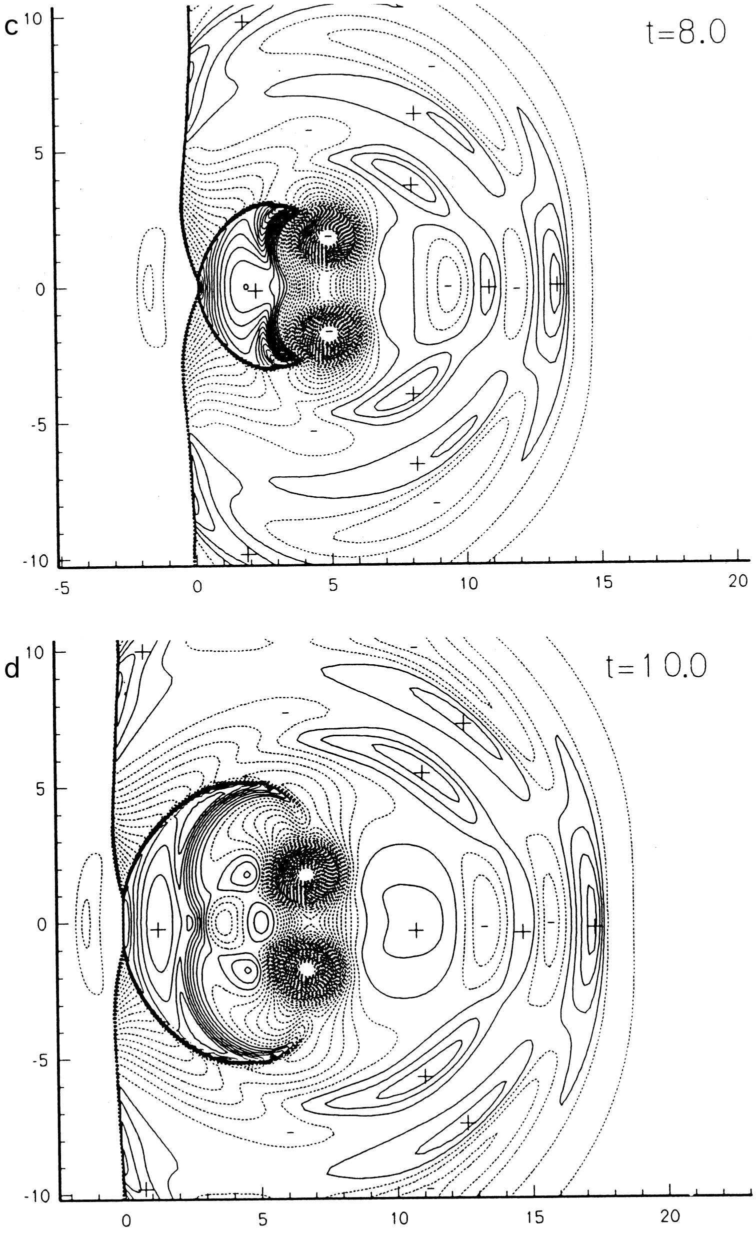

Figure 7 (*Continued*)

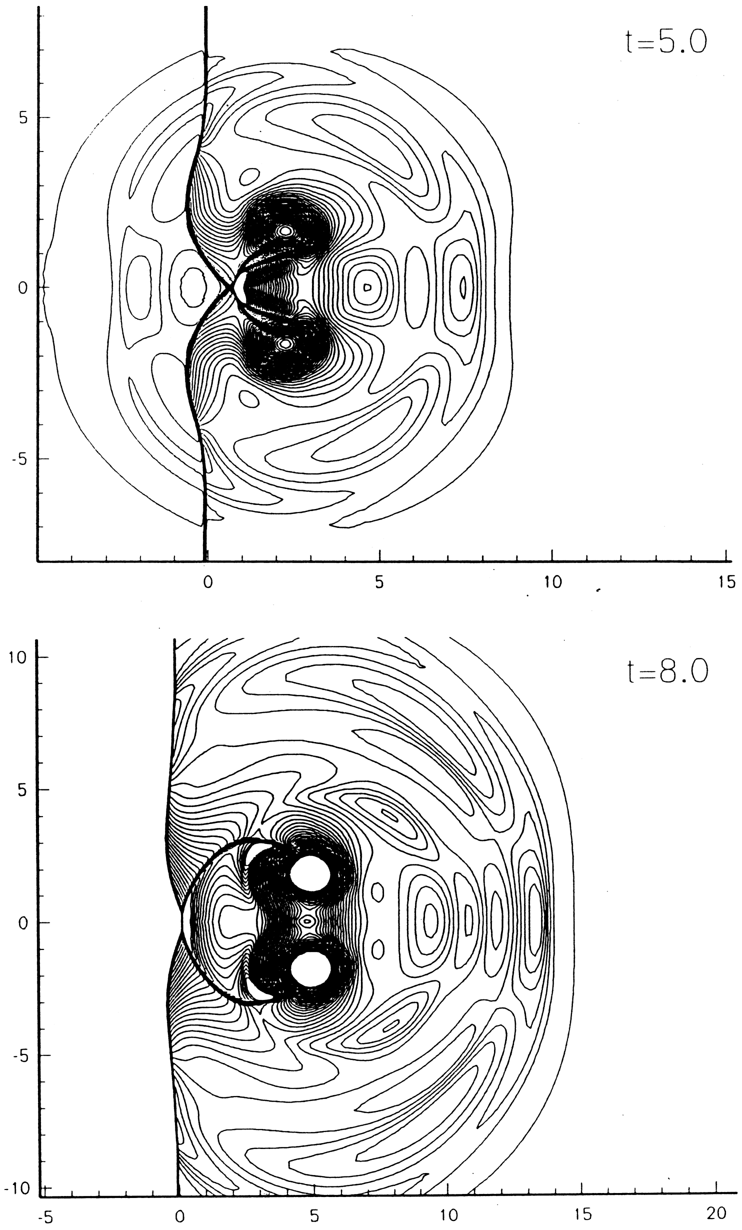

Figure 8. Density contours for case C: (a) $-0.8 \leq \rho \leq 1.5$, 70 levels; (b) $1.1 \leq \rho \leq 1.45$, 50 levels.

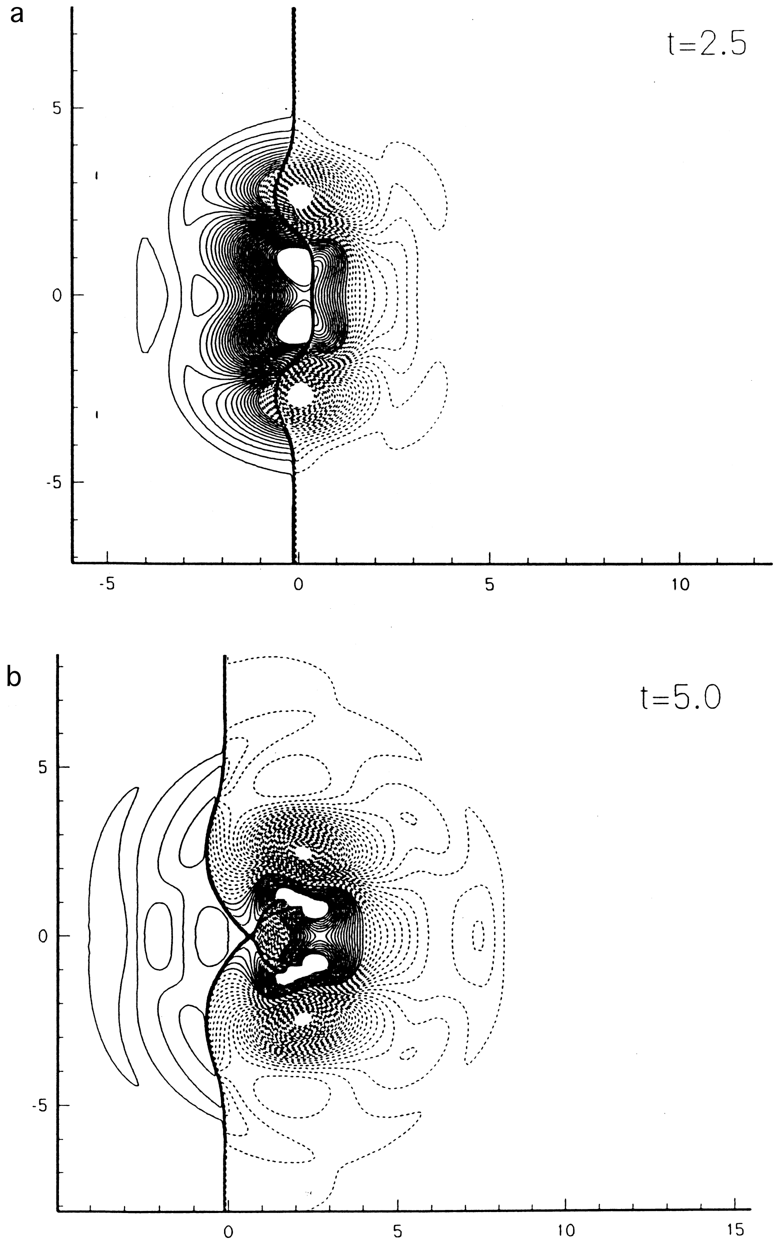

Figure 9. Mach number contours for case C: (a) $-0.5 \leq M_a - 1 \leq 0.7$, 80 levels; (b) $-0.6 \leq M_a - 1 \leq 0.3$, 60 levels; (c) $-0.5 \leq M_a - 1 \leq 0.4$, 60 levels; (d) $-0.6 \leq M_a - 1 \leq 0.4$, 60 levels.

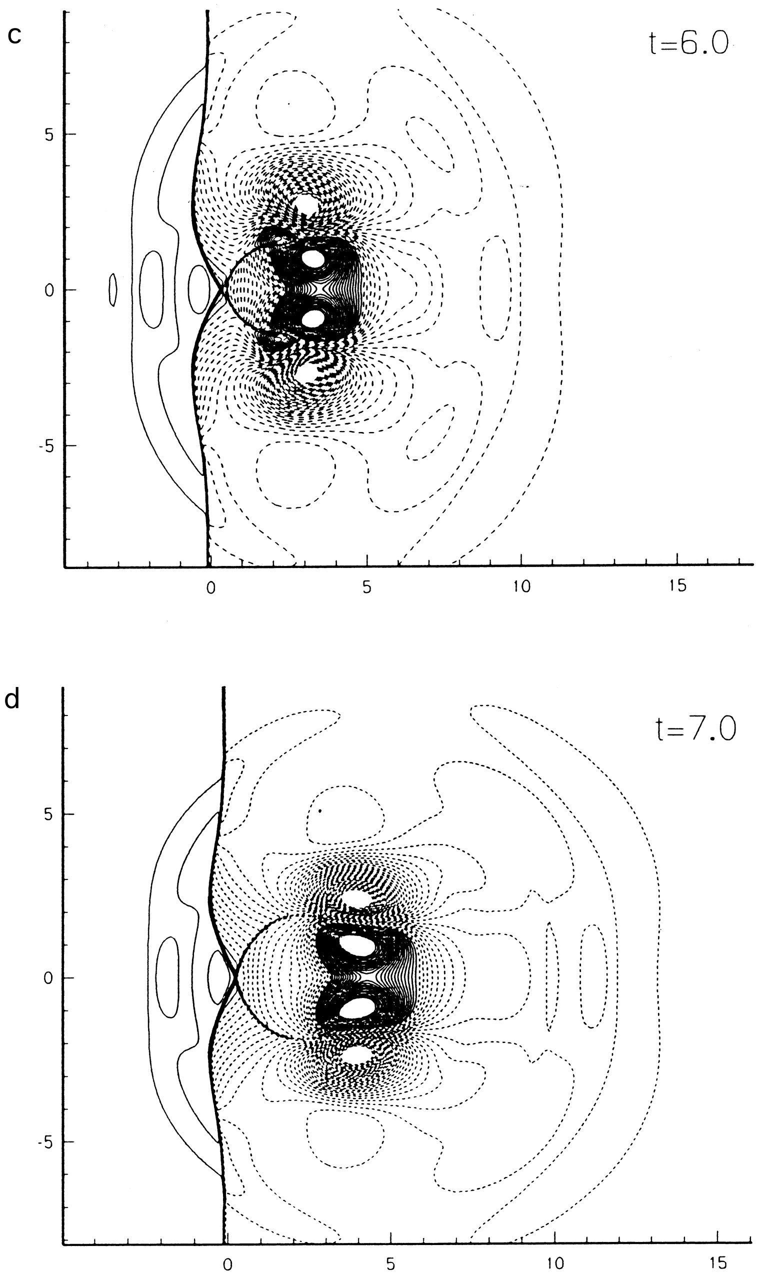

Figure 9 (*Continued*)

5.1. Computed results for case C

Consider case C, the computed pressure difference (sound field) at different times is given in Figure 7 and the density and the Mach number contours are given in Figures 8 and 9 respectively. Quite a large difference in structures compared with the single vortex–shock interaction is obtained near $y = 0$. From the sound field (Figure 7) we can see formation of the precursor and the sequential sounds. Comparing the pressure contours at $t = 5.0$ (Figure 7(b)) with the density contours at the same time in Figure 8(a) we see the difference near $y = 0$ between two vortices. They are slip lines. Schematic diagrams are given in Figure 10. The flow structures at early times of interaction can be analysed, as in Figure 6, for a single vortex–shock interaction, but there is a big difference downstream of the shock, near $y = 0$. Considering the flow field structures at early times of interaction near the central line, with similar analysis as in last section it can be seen that the deformation shock near $y = 0$ is toward upstream compared with the neighbouring points of the shock. According to the shock shape

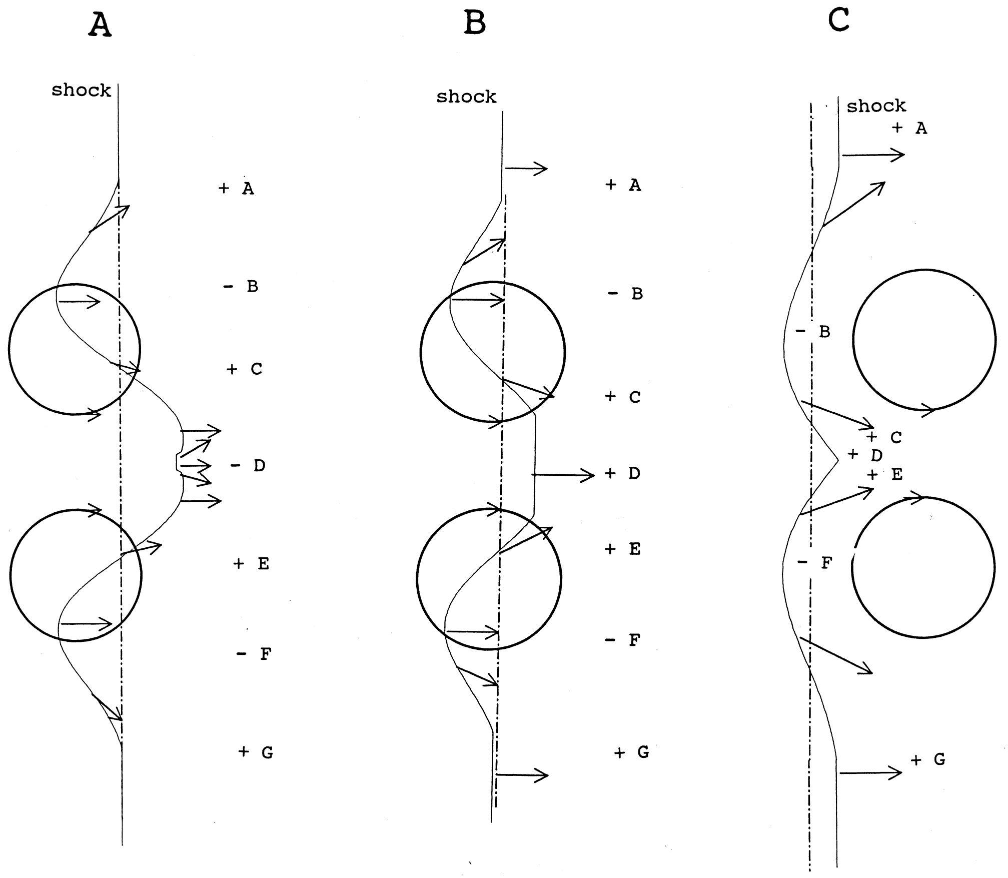

Figure 10. Schematic diagram of a pair vortices–shock interaction.

near $y = 0$ we know that in zone D (Figure 10(A)) behind the shock we have rarefaction and $\Delta P < 0$. The negative pressure difference can be seen in Figure 7(a) near $y = 0$ behind the shock at $t = 2.0$. This small rarefaction dissapears with time integration (Figure 10(B)). At a later time, the deformed shock is restored. The restoration is slower near the central line because of a two-side effect from the upper and lower vortices. Compression is obtained near point D (Figures 7(b) and 10(C)). We can also see compression near points A, C, E and G, rarefaction near points B and F at the early stages of interaction (Figure 10(A)). From Figure 7(b) it can be seen that there are two branches of secondary discontinuities that attach to the main shock, and each branch has its own sub-branches. With time integration the sub-branches merge into combined structures. In this case, the strength of the secondary discontinuities is much stronger than the case of a single vortex interaction. Therefore the secondary discontinuities may become shocks, and the triple point is formed at $t = 5.0$ for case C (Figure 7(b)). Comparing the density contours (Figure 8(a)) with the sound field (Figure 7(b)) we can see a pair of slip-line structures between two branches of discontinuities near $y = 0$.

From figures for Mach number contours we see that at the time when the centres of vortices are near the shock ($t = 2.5$) we have broken shock (Figure 9(a)). At a later stage (Figure 9(b)) we have a large supersonic region near the triple point. Inside the supersonic region between two outer sub-branches of discontinuities there are small subsonic regions. The outer

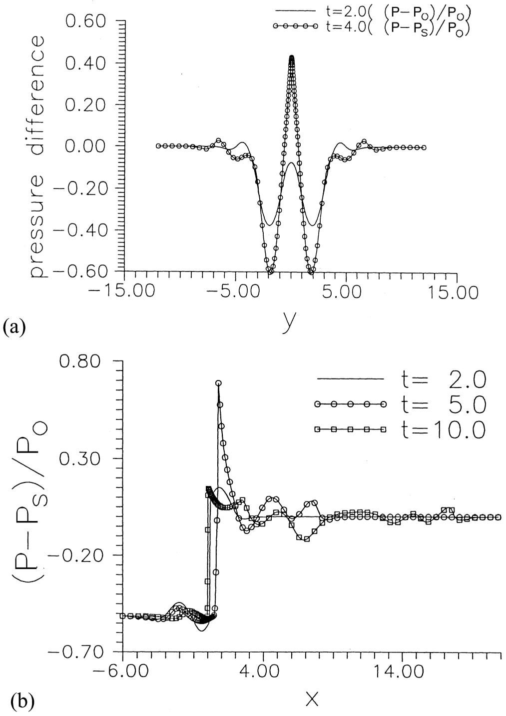

Figure 11. Pressure distribution for case C: (a) at $x = -0.54$ at $t = 2.0$ and $x = 1.4$ at $t = 4$ along the y-direction across the centres of vortices; (b) at $y = 0$ along the x-direction.

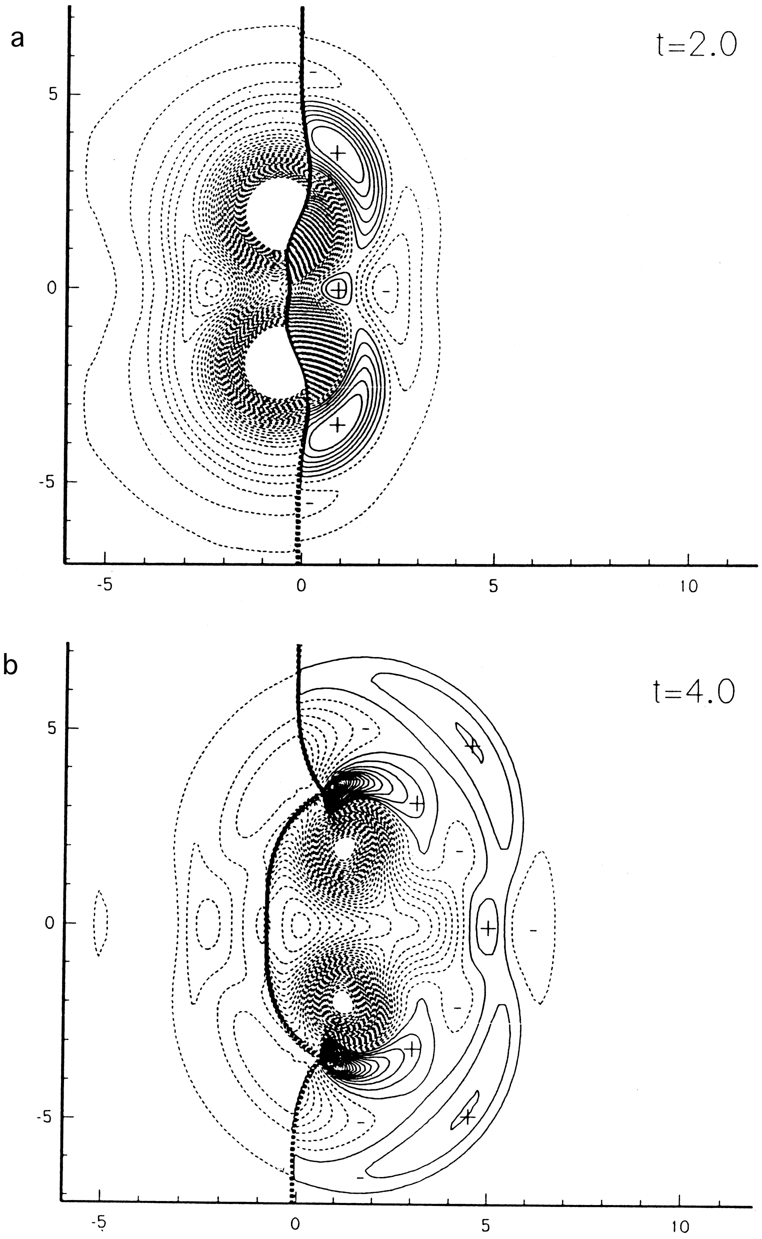

Figure 12. Time development of pressure field for case D: (a) $-0.75 \leq \Delta P \leq 0.05$, 80 levels; (b) $-0.55 \leq \Delta P \leq 0.95$, 80 levels; (c) $-0.5 \leq \Delta P \leq 0.3$, 60 levels; (d) $-0.5 \leq \Delta P \leq 0.15$, 60 levels.

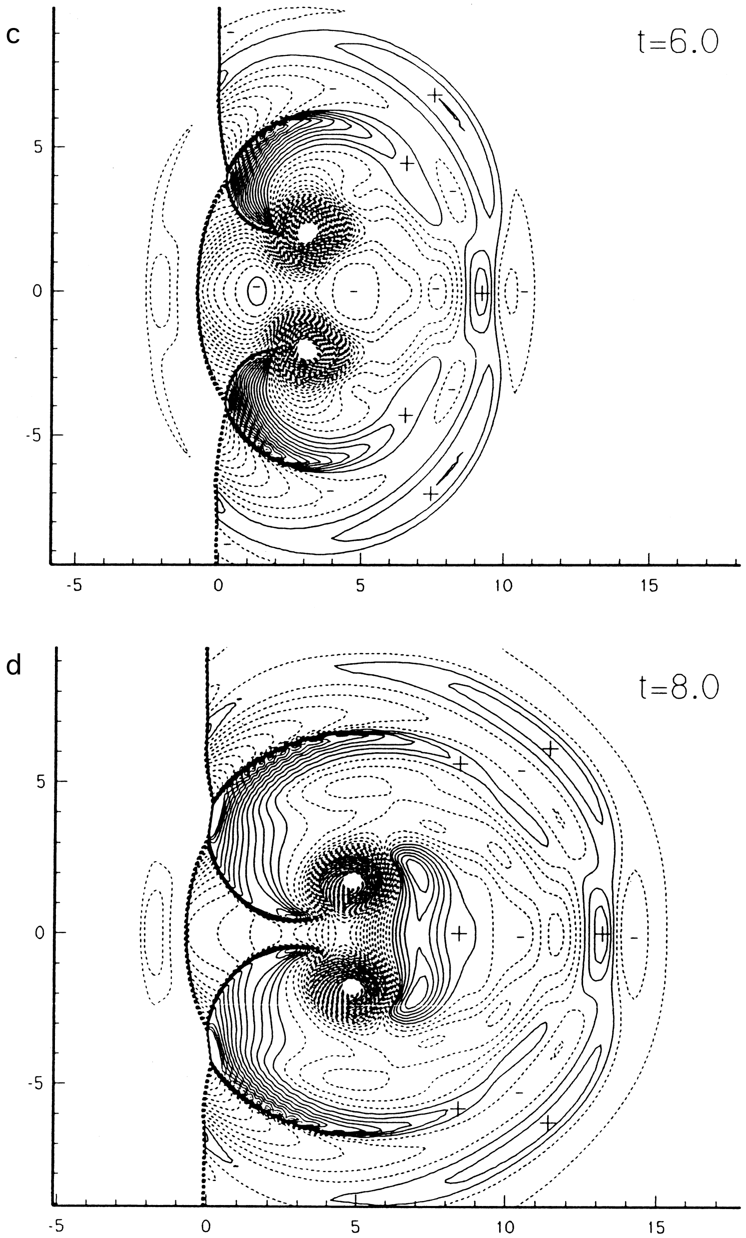

Figure 12 (*Continued*)

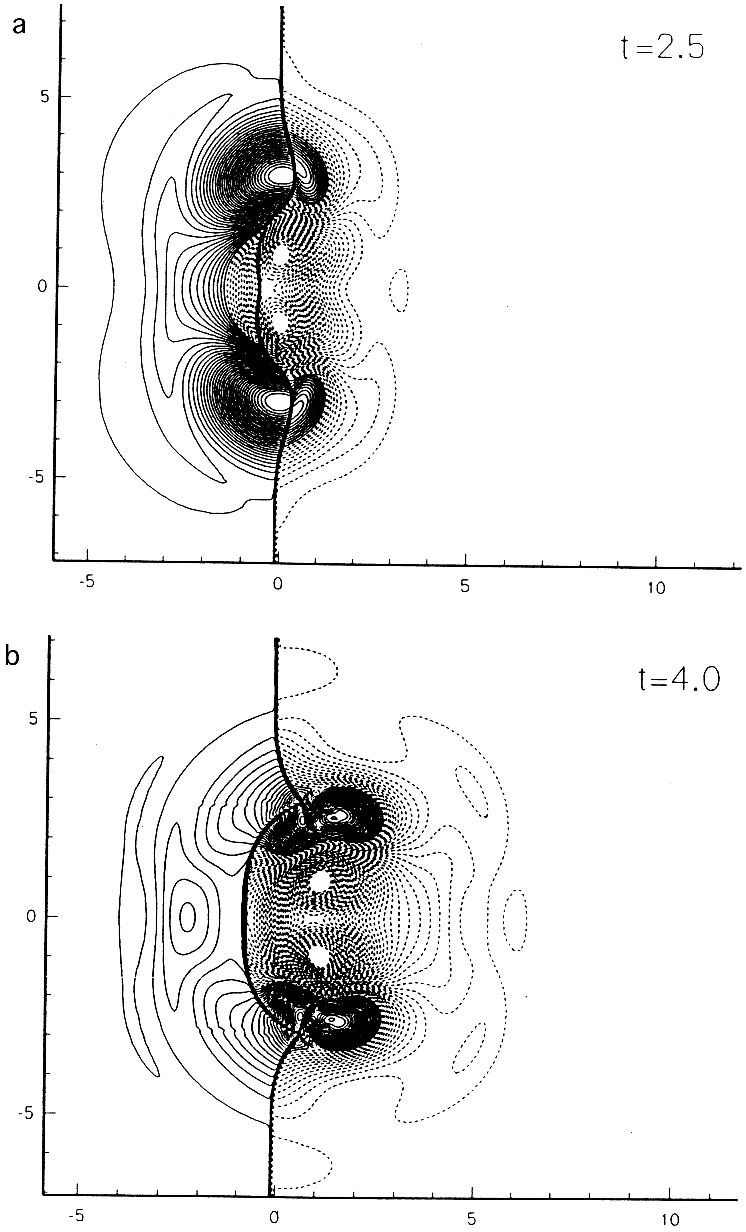

Figure 13. Mach number contours for case D: (a) $-0.6 \le M_a - 1 \le 0.7$, 80 levels; (b) $-0.6 \le M_a - 1 \le 0.4$, 80 levels; (c) $-0.4 \le M_a - 1 \le 0.3$, 60 levels; (d) $-0.5 \le M_a - 1 \le 0.35$, 60 levels.

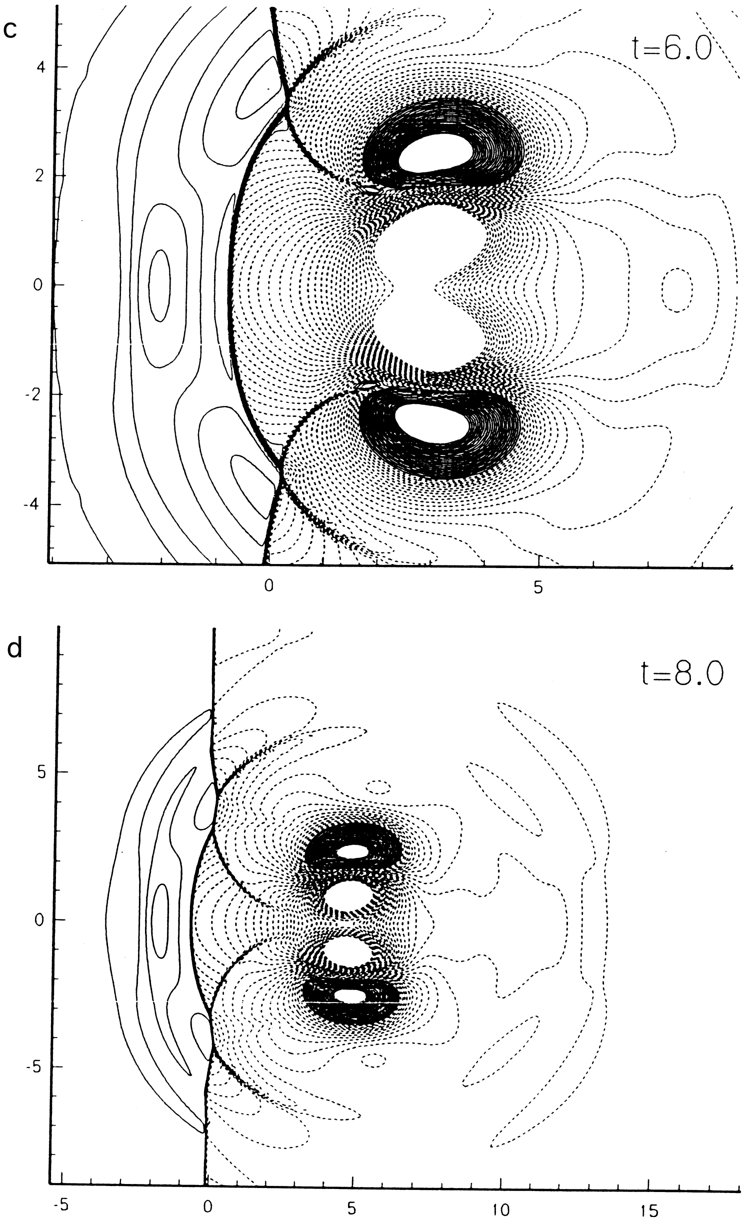

Figure 13 (*Continued*)

sub-branches may be reflecting shock because the flows in their upstream are supersonic. At a later time, the supersonic regions turn into two sub-regions, one near the triple point and another between two vortices (Figure 9(c)). Two ends of each reflecting discontinuity may be the shocks.

Figure 11(a) gives the variations of pressure difference $(P-P_\infty)/P_\infty$ at $t=2$ along the line $x=-0.54$, and $(P-P_s)/P_\infty$ at time $t=4$ along the line $x=1.4$ as a function of y, where the vortex centres are located at the corresponding points. From curves it can be seen that the disturbed region is enlarged after vortex–shock interaction. Figure 11(b) gives the variations of pressure difference $(P-P_\infty)/P_\infty$ along $y=0$ as a function of x at $t=2.0$, 5.0 and 10.0. From Figure 11 it can be seen that at time $t=5.0$ for case C, when the triple point is formed the pressure disturbance has the largest amplitude. From this figure we also can see the movement of the first (precursor) and second sound.

5.2. Computed results for case D

The computed results of sound fields and Mach number contours for case D are given in Figures 12 and 13 respectively. Formation of the sounds at the first stage of interaction can be analysed as for case C. From Figure 13, for the Mach number contours, we see that the shock is broken at $t=2.5$, and there is a large area with subsonic flow upstream of the shock. As discussed for the single vortex–shock interaction, it is the residue of what was a shock before interaction. We also see supersonic regions downstream of the shock (Figure 13(a)). This is because of the large tangential component of velocity. At $t=4.0$ we have two supersonic regions symmetrically located according to the axis $y=0$ (Figure 13(b)). At $t=6.0$ there are four supersonic regions, two of them are very small near the triple points.

6. CONCLUSION

A new high-order accurate method, the SCFDM, is analysed. From the analysis it is concluded that the SCFDM has better resolving efficiency than the traditional and compact difference methods. The SCFDM is used to approximate the compressible Navier–Stokes equations and simulate vortex–shock interactions. From computed results we can see the process of formation of the sounds and the reflecting discontinuities. It is noted that deformation of shock during the time of interaction produces complicated flow field structures. Simulation shows that for weak vortex–shock interactions, as computed in the present paper, the majority of reflecting discontinuities are not the shocks. The existence of reflecting shock depends on the strength of interaction. A peak in amplitude of pressure disturbance in the flow field is obtained during the time of formation of the triple points.

ACKNOWLEDGMENTS

This work is supported by the National Natural Science Foundation of China, and Key Project for Basic Research. The work was performed on computers of State Kay Laboratory of Scientific and Engineering Computing, Chinese Academy of Sciences.

REFERENCES

1. Rai MM, Moin P. Direct simulation of turbulent flow using finite-difference schemes. *Journal of Computational Physics* 1991; **96**(1): 15–53.
2. Lele SK. Compact finite difference schemes with spectral-like resolution. *Journal of Computational Physics* 1992; **13**: 16–142.
3. Dexun Fu, Yanwen Ma. Efficiency and accuracy of numerical methods for solving the aerodynamic equations. In *Numerical Methods in Fluid Dynamics*, *I. Proceedings of the International Symposium on Computational Fluid Dynamics*, *Nagoya*, Yasuhara M, Daiguji H, Oshima K (eds). Japan Society of Computational Fluid Dynamics: Tokyo, 1989; 78–85.
4. Dexun Fu, Yanwen Ma. A high order accurate difference scheme for complex flow fields. *Journal of Computational Physics* 1997; **134**: 1–15.
5. Dexun Fu, Yanwen Ma. High resolution schemes. In *Computational Fluid Dynamics Review 1995*, Hafez M, Oshima K (eds). Wiley: New York, 1995.
6. Yanwen Ma, Dexun Fu. Super compact finite difference method (SCFDM) with arbitrarily high accuracy. *Computational Fluid Dynamics Journal* 1996; **5**(2): 259–276.
7. Guichard L, Vervisch L, Doingo P. Two-dimensional weak shock–vortex interaction in a mixing zone. *AIAA Journal* 1995; **33**(10): 1797–1802.
8. Inoue O, Hattori Y. Sound generation by shock–vortex interactions. *Journal of Fluid Mechanics* 1999; **380**: 81–116.
9. Ellzey JL, Henneke MR. The Interaction of a shock with a vortex: shock distortion and the production of acoustic waves. *Physics and Fluids* 1995; **7**(1): 172–184.
10. Meadows KR, Kumar A, Hussaini MY. Computational study on the interaction between a vortex and a shock wave. *AIAA Journal* 1991; **29**(2): 174–179.
11. Chatterjee A, Povitsky A. Computational study of curved shock–vortex interaction. *International Journal for Numerical Methods in Fluids* 1999; **30**: 257–277.
12. Dosanjh DS, Weeks TM. Interaction of a starting vortex as well as a vortex street with a traveling shcok wave. *AIAA Journal* 1965; **3**: 216–273.